ACS APPLIED MATERIALS & INTERFACES

www.acsami.org

Research Article

Photonic Crystal Effects on Upconversion Enhancement of $LiErF_4$:0.5%Tm^{3+}@$LiYF_4$ for Noncontact Cholesterol Detection

Ling Zhang,‡ Songtao Hu,‡ Yang Lu, Bin Jiang, Xiaomin Liu,* Xiaodan Li, Xu Zhao, Xu Yan, Chenguang Wang, Xiaoteng Jia, Fengmin Liu, Biao Dong,* and Geyu Lu*

Cite This: *ACS Appl. Mater. Interfaces* 2022, 14, 428−438

Read Online

ACCESS | Metrics & More | Article Recommendations | Supporting Information

ABSTRACT: Cholesterol is a vital compound in maintenance for human health, and its concentration levels are tightly associated with various diseases. Therefore, accurate monitoring of cholesterol is of great significance in clinical diagnosis. Herein, we fabricated a noncontact biosensor based on photonic crystal-enhanced upconversion nanoparticles (UCNPs) for highly sensitive and interference-free cholesterol detection. By compounding $LiErF_4$:0.5%Tm^{3+}@$LiYF_4$ UCNPs with poly(methyl methacrylate) (PMMA) photonic crystals (OPCs), we were able to selectively tune the coupling of the photonic band gap to the excitation field and modulate the upconversion (UC) luminescence intensity, given the unique multi-wavelength excitation property of $LiErF_4$:0.5%Tm^{3+}@$LiYF_4$. A 48.5-fold enhancement of the monochromatic red UC emission was ultimately achieved at 980 nm excitation, ensuring improved detection sensitivity. Based on the principle of quenching of the intense monochromic red UC emission by the oxidation products of 3,3′,5,5′-tetramethylbenzidine (TMB) yielded from the cholesterol cascade reactions, the biosensor has a detection limit of 1.6 μM for cholesterol with excellent specificity and stability. In addition, the testing results of the as-designed biosensor in patients are highly consistent with clinical diagnostic data, providing a sensitive, reliable, reusable, interference-free, and alternative strategy for clinical cholesterol detection.

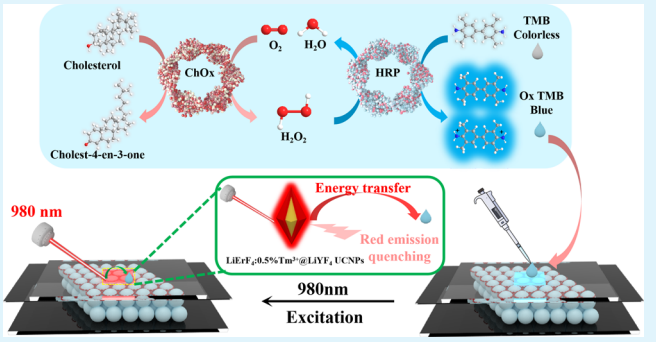

KEYWORDS: *photonic crystal effect, $LiErF_4$, upconversion emission enhancement, cholesterol detection, red emission quenching, energy transfer*

1. INTRODUCTION

Cholesterol is an essential substance that is indispensable for human tissue cells and plays a critical role in basic cellular life activities. High cholesterol levels can lead to atherosclerosis, cardiovascular, and cerebrovascular diseases, while low cholesterol levels increase the risk of brain hemorrhage and reduce the body's resistance. Therefore, the determination of cholesterol is of great practical significance for maintaining good health. Many methods have been exploited for cholesterol detection, such as colorimetry,[1−3] high-performance liquid chromatography,[4] electrochemical analysis,[5,6] chemiluminescence,[7] and fluorescence-based assays.[8−10] Among them, fluorescence technology has become an important method for real-time detection of cholesterol in living cells, serum, and tissues.[11−13] Although many advances have been made in this method, majority of luminescent materials or organic dyes are excited in the UV−Vis region, in which biomolecules with strong absorption are prone to biological autofluorescence, significantly affecting detection sensitivity. Therefore, it still remains a challenge to explore a highly sensitive, interference-free, and recyclable fluorescence approach to determine cholesterol levels.

As an effective option for fluorescent probes, upconversion nanoparticles (UCNPs) have attracted much attention in the construction of fluorescence-based sensors due to their advantages of no autofluorescence, no bleaching phenomenon, and deep penetration depth.[14−20] However, the low fluorescence quantum yield due to the small absorption cross section of UCNPs limits their further application in biofluorescent sensors. Therefore, it is important and necessary to increase the intensity of upconversion (UC) luminescence to enhance the sensitivity in bioassay applications. There are several ways to enhance the UC luminescence, including (i) selecting effective crystalline phases and substrates;[21,22] (ii)

Received: November 10, 2021
Accepted: December 22, 2021
Published: December 29, 2021

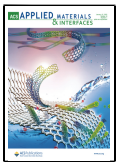

constructing core−shell structures to separate the luminescence center from the quenching center;[23−25] and (iii) enhancing by external fields such as the surface plasmon resonance effect or photonic crystal effect. Among them, enhancements of tens of magnitudes of UC luminescence have been obtained by the external field.[26,27] The surface plasmon resonance effect of noble metal structures such as gold or silver can be used to enhance the local light field,[28] but is prone to emission quenching at small distances of less than 10 nm from the metal particle surface. In contrast, the coupling effect between the photonic crystal and the excitation field can be exploited to enhance UC luminescence without the quenching effect.[29,30] The photonic crystal is a periodic dielectric structure with a photonic band gap (PBG), which means that the wavelength of a certain frequency range cannot propagate in this periodic structure, i.e., the structure itself has a "forbidden band". The PBG can affect the interaction between light and luminescent material, which in turn affects the optical absorption and emission characteristics of materials to achieve the enhancement of UC luminescence. Given this, the development of fluorescent probes or systems based on photonic crystal-enhanced UCNPs for highly sensitive detection of cholesterol is of great practical interest and application prospects. Unfortunately, little related work has been reported yet.

In this paper, $LiErF_4$:0.5%Tm^{3+}@$LiYF_4$ UCNPs were selected to compound with poly(methyl methacrylate) (PMMA) opal photonic crystals (OPCs) to explore the enhancement of fluorescence intensity of the $LiErF_4$ system by the photonic crystal effect. The fluorescence enhancement-based sensor was then constructed for cholesterol detection. In contrast to traditional co-doped systems (Yb^{3+}/Er^{3+}) required to be excited at a specific wavelength (∼980 nm),[27,31] these $LiErF_4$:0.5%Tm^{3+}@$LiYF_4$ UCNPs can exhibit an intense red UC emission (∼660 nm) under multi-wavelength (∼808, ∼980, and ∼1530 nm) excitation attributed to the ladder-like energy structure of the Er^{3+} ions.[32] The unique multi-wavelength excitation property provides an excellent opportunity to achieve enhanced luminescence by selectively modulating the coupling of the photonic band gap to the excitation field. Through the photonic crystal field enhancement effect, a brighter monochromatic red UC emission with 48.5 times enhancement at 980 nm excitation was ultimately obtained. A noncontact cholesterol sensor was further established based on the quenching of the intense monochromic red UC emission by the oxidation products of 3,3′,5,5′-tetramethylbenzidine (TMB) derived from the cholesterol cascade reactions. The biosensor exhibits superior specificity and stability with an LOD of 1.6 μM for cholesterol. The potential of the designed biosensor for cholesterol detection in patients has also been validated with results that are highly consistent with clinical diagnostic data, demonstrating a reliable, reusable, interference-free, highly sensitive, and alternative strategy for clinical cholesterol detection.

2. EXPERIMENTAL SECTION

Materials and instruments are detailed in the Supporting Information.

2.1. Synthesis of $LiErF_4$:0.5%Tm^{3+} Core UCNPs. The UCNPs were synthesized in reference to the typical solvothermal method.[33] $TmCl_3·6H_2O$ (0.005 mmol), $ErCl_3·6H_2O$ (0.995 mmol), 14 mL of ODE, and 6 mL of OA were mixed in a 50 mL flask and stirred for 30 min. The above solution was heated to 160 °C for 40 min and then cooled to 50 °C. A 10 mL methanol solution containing LiOH (2.500 mmol) and NH_4F (4.000 mmol) was introduced and heated to 70 °C for 40 min. Then, the mixture was heated to 300 °C for 90 min and cooled to 50 °C, and the core UCNPs were obtained after washing by centrifugation with acetone and ethanol. Finally, the core UCNPs were dissolved in 8 mL of cyclohexane to be used. Notice that continuous N_2 flow and stirring were necessary throughout the experiment.

2.2. Synthesis of $LiErF_4$:0.5%Tm^{3+}@$LiYF_4$ Core−Shell UCNPs. A mixture of $YCl_3·6H_2O$ (0.750 mmol), 10 mL of ODE, and 5 mL of OA were mixed in a 50 mL flask and stirred for 30 min. The above solution was heated to 160 °C for 40 min and then cooled to 50 °C. Next, 4 mL of cyclohexane containing $LiErF_4$:0.5%Tm^{3+} core UCNPs was introduced and heated to 85 °C for 30 min and then cooled down to 50 °C. A 5 mL methanol solution containing LiOH (1.875 mmol) and NH_4F (3.000 mmol) was added and heated to 70 °C for 30 min. Then, the solution was heated to 300 °C for 60 min and cooled to 50 °C; the core−shell UCNPs were obtained after washing by centrifugation with acetone and ethanol. Finally, the core−shell UCNPs were dissolved in 4 mL of cyclohexane to be used.

2.3. Preparation of PMMA OPCs. PMMA OPCs were obtained by a vertical deposition method from monodisperse PMMA microspheres self-assembled onto a glass substrate.[29] The PBG positions of OPCs were finely tuned by controlling the diameter of PMMA beads. OPCs manufactured from PMMA microspheres of ∼345, ∼424, and ∼667 nm in diameter were denoted as the OPCs-808, OPCs-980, and OPCs-1530, respectively. First, 20 mL of methyl methacrylate (MMA) was cleaned seven times with 100 mL of NaOH (5 mg mL^{-1}), then 6 mL of cleaned MMA and 80 mL of deionized water were mixed and heated, 36 mg of $K_2S_2O_8$ was added, and the reaction was carried out at 90 °C for 90 min to obtain a monodisperse solution of PMMA microspheres. The cleaned slides were inserted vertically into the PMMA microsphere liquid, kept at 30−40 °C for 24 h, dried, and subsequently heated to 120−140 °C for 60 min, thus obtaining the PMMA opal crystal structure.

2.4. Fabrication of $LiErF_4$:0.5%Tm^{3+}@$LiYF_4$ UCNPs with PMMA OPCs Hybrids and Construction of the Noncontact Cholesterol Sensor. The composite films were prepared by the spin-spray method. Briefly, as-prepared OPCs films were fixed on a spin table. Then, 1 mL of 0.8 mmol mL^{-1} $LiErF_4$:0.5%Tm^{3+}@$LiYF_4$ UCNPs cyclohexane solution was sprayed onto the OPCs films or glass through a spray gun, $LiErF_4$:0.5%Tm^{3+}@$LiYF_4$ UCNPs will self-assemble onto the surface of OPCs films or glass with the evaporation of cyclohexane. After depositing $LiErF_4$:0.5%Tm^{3+}@$LiYF_4$ UCNPs on photonic crystal films and glass, we denoted the corresponding films as OPCs-808/UCNPs, OPCs-980/UCNPs, OPCs-1530/UCNPs, and glass/UCNPs, respectively. For cholesterol detection, we also designed a noncontact cholesterol sensor, as shown in Scheme 2a. A 100 μm ultrathin glass sheet was covered with the OPCs/UCNPs hybrid film to isolate the liquid to be measured, and an acrylic plate with a hole was glued on top of it to hold the liquid to be measured.

2.5. Detection of Cholesterol. Phosphate buffer (100 μL, 0.1 M, pH 7.0), cholesterol oxidase (100 μL, ChOx, 0.16 U mL^{-1}), deionized water (200 μL), and different concentrations of cholesterol (100 μL) (dissolved in methanol) were mixed and incubated at 37 °C for 30 min, and then acetate buffer (100 μL, 0.1 M, pH 4.0), horseradish peroxidase (100 μL, HRP, 6 mU mL^{-1}), TMB (100 μL, 20 mM), and deionized water (1.2 mL) were added to the above mixture at 37 °C for 30 min. Then, the UC emission spectra of $LiErF_4$:0.5%Tm^{3+}@$LiYF_4$ UCNPs on the noncontact OPCs-980/UCNPs cholesterol sensor dropped with the above mixture were monitored. To test the selectivity of cholesterol detection, glucose, urea, uric acid, ascorbic acid, cysteine, and $MgCl_2$ (2 mM) were added to the reaction solution as substitutes for cholesterol, and then, the same cholesterol assay procedure was performed separately.

2.6. Detection of Cholesterol in Human Serum. To determine the total cholesterol level in human serum, cholesterol esterase (ChE) was used to hydrolyze cholesterol ester into cholesterol. Details of the operation are as follows: 100 μL of phosphate buffer (0.1 M, pH 7.0), 100 μL of ChOx (0.16 U mL^{-1}), 100 μL of ChE (0.2 U mL^{-1}), 100 μL of clinical patient serum (provided from the Department of

https://doi.org/10.1021/acsami.1c21834
ACS Appl. Mater. Interfaces 2022, 14, 428−438

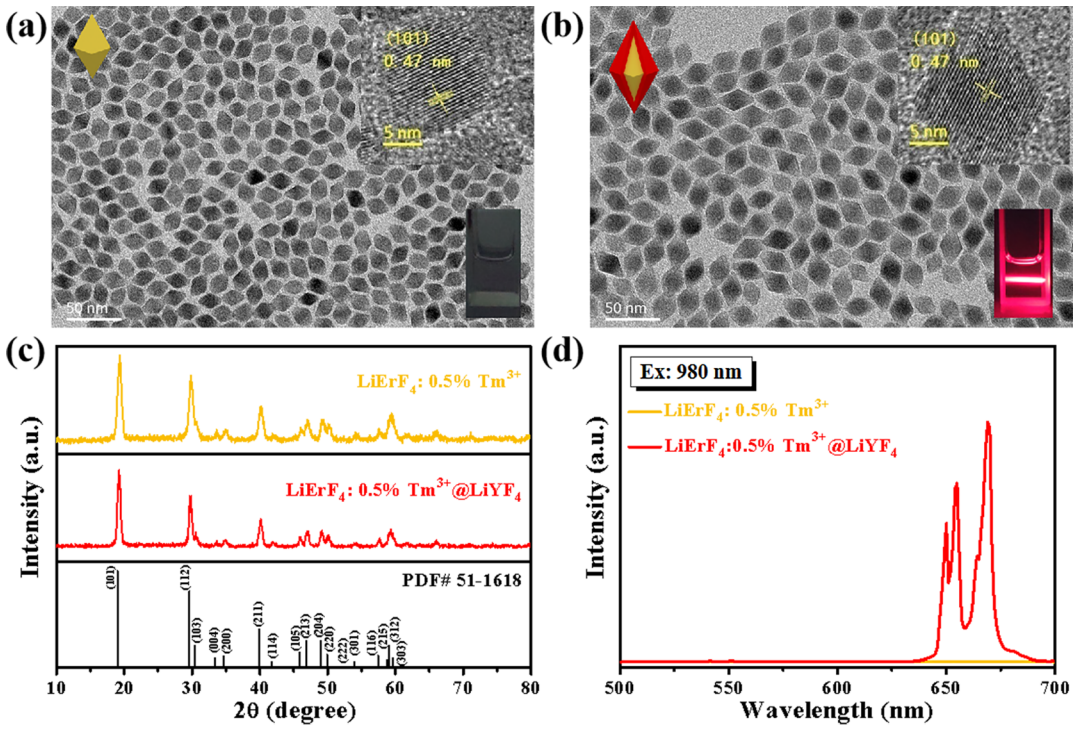

Figure 1. TEM images of (a) the $LiErF_4$:0.5%Tm^{3+} core and (b) $LiErF_4$:0.5%Tm^{3+}@$LiYF_4$ core−shell UCNPs. (c) XRD patterns of UCNPs. (d) UC emission spectra of UCNPs dissolved in cyclohexane under 980 nm excitation (5.50 W cm^{-2}).

Respiratory Medicine, The First Hospital, Jilin University) diluted 50-fold with deionized water, and 100 μL of methanol were mixed and incubated at 37 °C for 30 min. The next procedures are the same as those in Section 2.5.

3. RESULTS AND DISCUSSION

3.1. Characterization of the $LiErF_4$:0.5%Tm^{3+} Core and $LiErF_4$:0.5%Tm^{3+}@$LiYF_4$ Core−Shell UCNPs. The $LiErF_4$:0.5%Tm^{3+} core and $LiErF_4$:0.5%Tm^{3+}@$LiYF_4$ core−shell UCNPs have been successfully synthesized by a high-temperature solvothermal method as reported previously.[33] Figure 1a,b shows the TEM images of UCNPs. It can be seen from the figure that the UCNPs are in the form of tetragonal bipyramid. The average sizes of core and core−shell UCNPs are approximately (14.8 ± 1.1) nm × (22.1 ± 0.9) nm (short length × long diagonal length) and (19.8 ± 1.3) nm × (33.5 ± 1.4) nm, respectively. The XRD patterns of UCNPs are shown in Figure 2c, which are consistent with a pure tetragonal phase (JCPDS no. 51-1618). The resolution TEM images inserted in Figure 1a,b show clear lattice fringes with a fringe spacing of approximately 0.47 nm, which corresponds to the (101) crystal plane spacing of tetragonal $LiErF_4$. We next investigated the UC luminescence properties of UCNPs under the 980 nm excitation (5.50 W cm^{-2}), as shown in Figure 1d. The results show a complete absence of emission from the $LiErF_4$:0.5% Tm^{3+} core due to the concentration quenching effect. However, the bright and near-monochromatic red UC emission of the UCNPs could be attained by coating an inert shell $LiYF_4$ to passivate the surface defects and thus eliminate the concentration quenching. In contrast to conventional co-doping systems stimulated by only a certain wavelength, the $LiErF_4$:0.5%Tm^{3+}@$LiYF_4$ core−shell UCNPs exhibit a monochromic red UC emission (~660 nm, $^4F_{9/2} \rightarrow {}^4I_{15/2}$) under multi-band excitations (~808, ~980, and ~1530 nm), as indicated in Figure 1d, Figure S1, and Figure S2. The luminescence mechanism was described in detail in our previous work.[32]

3.2. Morphology and Optical Properties of PMMA OPCs/$LiErF_4$:0.5%Tm^{3+}@$LiYF_4$ (OPCs/UCNPs) Hybrid Films. Based on the multi-wavelength excitation characteristic of $LiErF_4$:0.5%Tm^{3+}@$LiYF_4$ UCNPs, we focus on the effect of photonic crystals on enhancing the UC emission of $LiErF_4$:0.5%Tm^{3+}@$LiYF_4$ by modulating the matching of different band gap positions of photonic crystals with the excitation wavelengths of UCNPs. First, PMMA OPCs were successfully fabricated on glass substrates by a vertical deposition method, and then $LiErF_4$:0.5%Tm^{3+}@$LiYF_4$ UCNPs were compounded onto the OPCs by the spin-spray method to prepare the composite films (Scheme 1). The morphologies of the OPCs fabricated from individual PMMA microspheres of ~345, ~424, and ~667 nm diameters, respectively, were investigated by SEM, as shown in Figure 2a−c. The packed PMMA microspheres self-assemble into a highly ordered face-centered cubic (fcc) structure, where the (111) plane is parallel to the surface of the glass substrate. It can also be seen from the inset in Figure 2g that the OPCs films show different colors under room lighting, mainly because the OPCs films have different reflective wavelengths that are determined by the distance between the periodically arranged PMMA spheres.[34] Figure 2g shows the transmittance spectra of various OPCs tested at a normal to the substrate (θ = 0°). The transmittance spectra show that the OPCs present a deep and narrow PBG. The PBG positions of OPCs made of periodic arrangements of PMMA microspheres with dimensions of ~345, ~424, and ~667 nm are located at ~801, ~969, and ~1521 nm, respectively. We denote these three different OPCs as OPCs-808, OPCs-980, and OPCs-1530. With the increase in microsphere sizes, the PBG position of OPCs shifts significantly toward the long wavelength. In theory, the PBG

https://doi.org/10.1021/acsami.1c21834
ACS Appl. Mater. Interfaces 2022, 14, 428−438

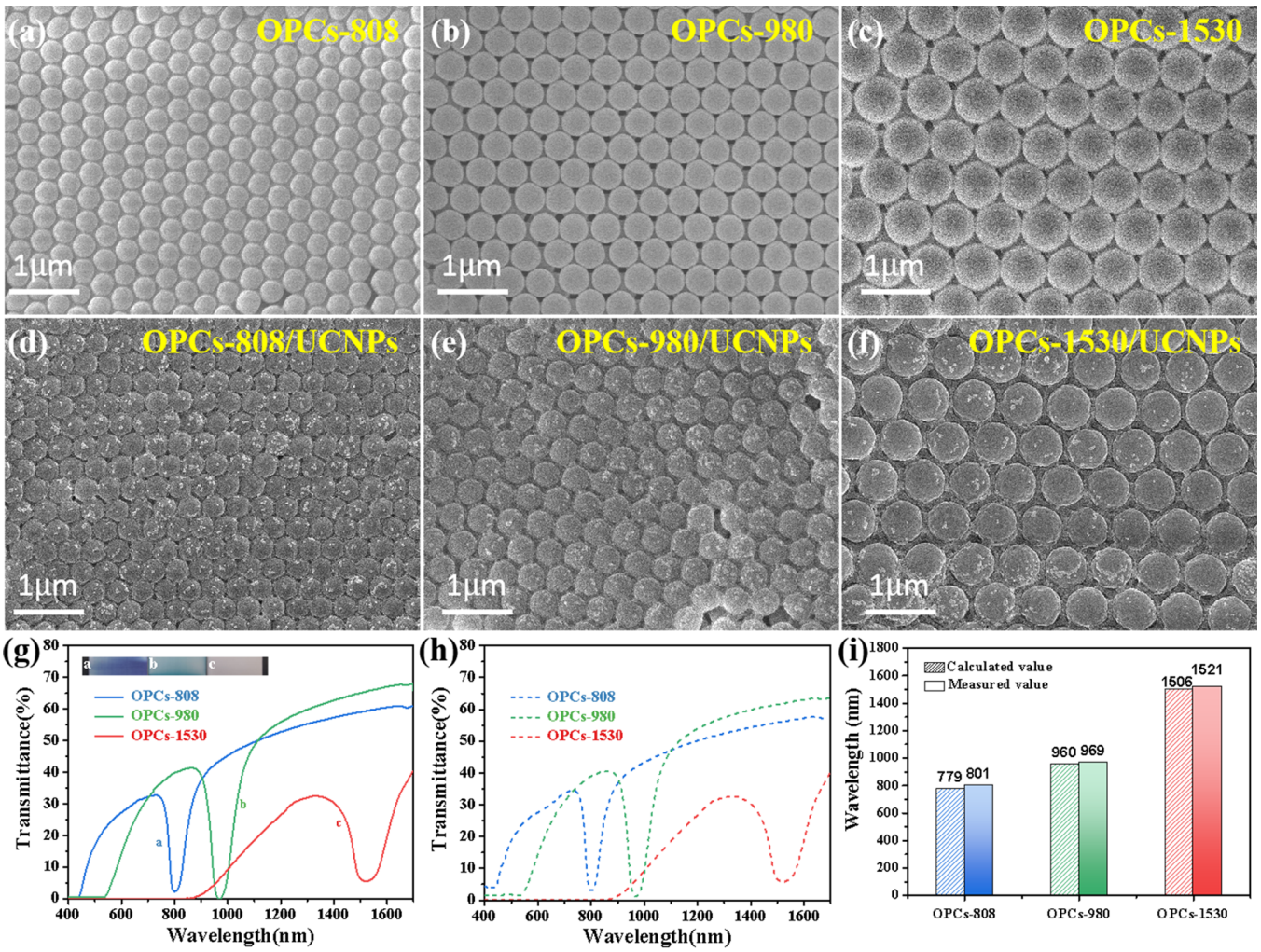

Figure 2. (a–c) SEM images of various OPCs. (d–f) SEM images of various OPCs/UCNPs hybrids. Transmittance spectra of the OPCs (g) before and (h) after the deposition of $LiErF_4$:0.5%Tm^{3+}@$LiYF_4$ UCNPs. The inset shows that the OPCs films display different colors under room illumination. (i) Comparison of actual measured values of photonic band gap positions with theoretically calculated values based on Bragg's law.

Scheme 1. Formation Process for OPCs/UCNPs Hybrids

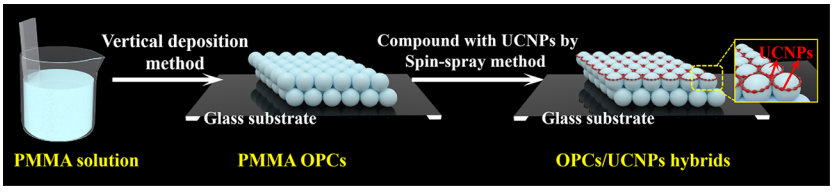

position of fcc PMMA could be well depicted by the modified Bragg's law:[34−37]

$$\lambda = 2\sqrt{2/3}\,D(n_{eff}^2 - \sin^2\theta)^{1/2} \quad (1)$$

$$n_{eff}^2 = n_{PMMA}^2 V_{PMMA} + n_{air}^2 V_{air} \quad (2)$$

λ is the center wavelength of the PBG position. D is the center-to-center distance between the microspheres, and the diameter of PMMA microsphere was used for D in the calculation. θ is the angle between the incident light and the normal to the substrate surface; $\theta = 0°$ was used in the calculation. n_{eff} is the effective refractive index. Here, n_{PMMA} and n_{air} are the refractive indices of PMMA microspheres and the air, respectively, where $n_{PMMA} = 1.494$ and $n_{air} = 1.000$ were used in the calculation. V_{PMMA} and V_{air} are the volume fractions of the PMMA microspheres and the air, which are approximately 74 and 26%, respectively. The n_{eff} value was calculated to be 1.383. Based on the above data, the PBG positions for all the OPCs were calculated. Figure 2i shows a comparison of the measured PBG positions with the PBG positions calculated according to Bragg's law. The results show that the measured values are slightly larger than the calculated values. In the calculation, we have replaced D (i.e., the center-to-center distance between the microspheres) with the diameter of PMMA. Figure 2a–c shows that there is a small gap among the PMMA microspheres so that the actual value of D is larger than the diameter of the microspheres, resulting in a smaller theoretical value than the measured value, but the difference is not significant.

https://doi.org/10.1021/acsami.1c21834
ACS Appl. Mater. Interfaces 2022, 14, 428−438

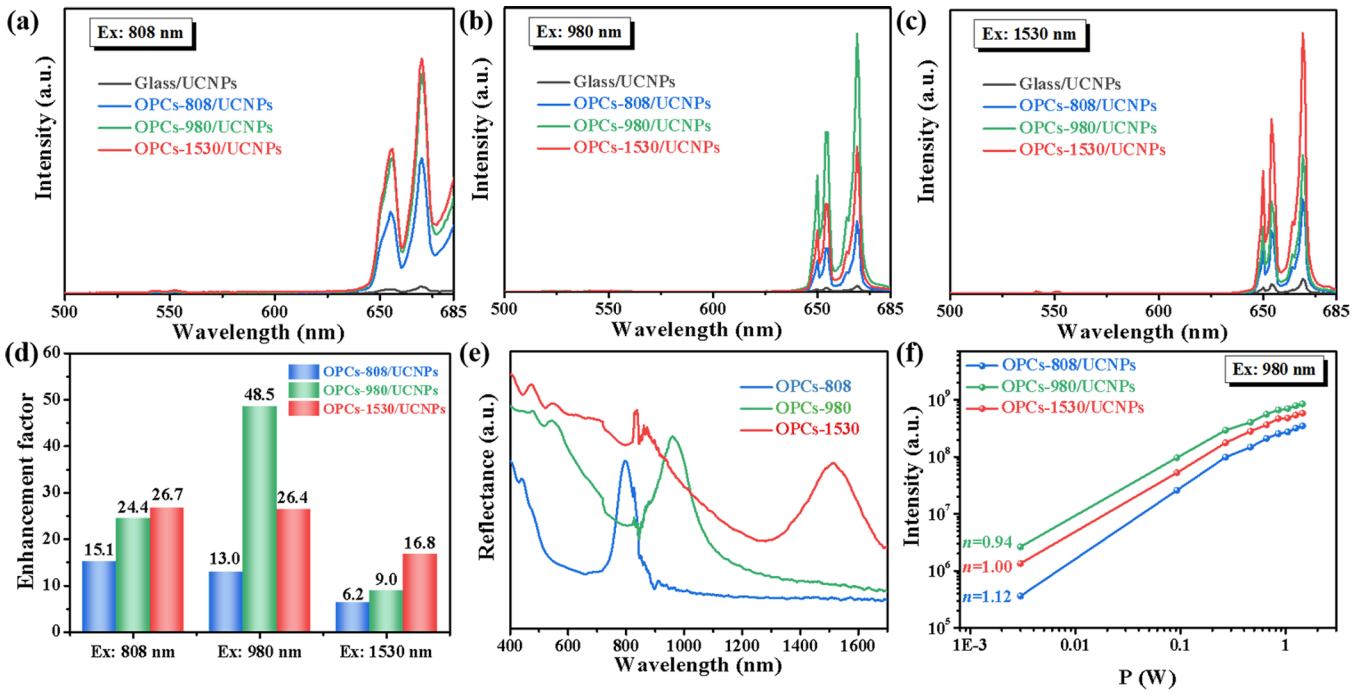

Figure 3. UC emission spectra of four types of luminescent films under (a) 808 nm (10.36 W cm^{-2}), (b) 980 nm (2.3 W cm^{-2}), and (c) 1530 nm (1.34 W cm^{-2}) excitation. (d) Enhancement factor (EF) values of different OPCs/UCNPs hybrids under 808, 980, and 1530 nm excitation. (e) Reflectance spectra of OPCs/UCNPs hybrids. (f) Power-dependent red UC emission integrated intensity of the $^4F_{9/2} \rightarrow {}^4I_{15/2}$ transition of Er^{3+} on OPCs/UCNPs hybrids under the 980 nm excitation (the integrated range is ~640−680 nm).

To explore the effect of the PBG on the UC emission characteristics of the UCNPs, $LiErF_4$:0.5%Tm^{3+}@$LiYF_4$ UCNPs were further deposited on the surfaces of various photonic crystals and glass. Figure 2d−f shows the SEM images of OPCs films compounded with $LiErF_4$:0.5%Tm^{3+}@$LiYF_4$ UCNPs, and it can be seen that the UCNPs are regularly embedded in the surface gaps of the PMMA microspheres over a large area. The driving force for the formation of this structure should be ascribed to the electrostatic attraction between the PMMA microspheres and the $LiErF_4$:0.5%Tm^{3+}@$LiYF_4$ UCNPs during the volatilization of the solvent (cyclohexane). The force drives the UCNPs toward the lowest potential energy on the surface of the PMMA microspheres. The transmittance spectra of OPCs/UCNPs hybrids are shown in Figure 2h, and the results show that the PBG positions of OPCs do not shift after the deposition of UCNPs, indicating that the deposition of $LiErF_4$:0.5%Tm^{3+}@$LiYF_4$ UCNPs on the OPCs surface does not affect the position of the PBG.

3.3. UC Emission Enhancement and Mechanism of $LiErF_4$:0.5%Tm^{3+}@$LiYF_4$ UCNPs by the PMMA OPCs/$LiErF_4$:0.5%Tm^{3+}@$LiYF_4$ (OPCs/UCNPs) Hybrids. To investigate the effect of the PBG on the UC emission properties of $LiErF_4$:0.5%Tm^{3+}@$LiYF_4$, the UC emission spectra of UCNPs on various OPCs films as well as on glass substrates under the 808 (10.36 W cm^{-2}), 980 (2.3 W cm^{-2}), and 1530 (1.34 W cm^{-2}) nm excitation were examined. As indicated in Figure 3a−c, the bright and near-monochromatic red (~660 nm) UC emission assigned to the $^4F_{9/2} \rightarrow {}^4I_{15/2}$ transition of Er^{3+} in $LiErF_4$:0.5%Tm^{3+}@$LiYF_4$ UCNPs was observed. Meanwhile, the UC emission of $LiErF_4$:0.5%Tm^{3+}@$LiYF_4$ UCNPs on various OPCs films was enhanced to various degrees compared to the UCNPs on the glass substrate, whereby the corresponding enhancement factor (EF) values for the red UC emission were also obtained. Here, the EF is the ratio of the integrated intensity of the red UC emission (~640−680 nm) on various OPCs/UCNPs films to the intensity on the glass film (control film), as shown in Figure 3d. The EF values of the OPCs/UCNPs composite films varied with the PBG position from 6.2 to 48.5 times under the excitation of 980 and 1530 nm. The maximum enhancements of 48.5- and 16.8-fold were obtained for OPCs-980 and OPCs-1530, respectively, only when the excitation field wavelength matched well with the PBG position of OPCs. As the PBG position of the OPCs gradually deviates from the excitation field wavelength of UCNPs, the EF values of the red UC emission on the corresponding composite film also decrease rapidly. This indicates that the coupling between the OPCs and the excitation field of the UCNPs is the strongest. The UC luminescence enhancement observed on OPCs/UCNPs composite films at other PBG positions is mainly due to light amplification caused by random scattering from the surface of PMMA microspheres.

However, at 808 nm excitation, the enhancement of OPCs-980 and OPCs-1530 is stronger than that of OPCs-808, although the PBG position of OPCs-808 best matches the wavelength of the excitation field. To explain this phenomenon, we tested the reflectance spectra of several OPCs, as shown in Figure 3e. The results show that OPCs-980 and OPCs-1530 have a relatively high reflectance at ~808 nm, which can lead to a larger enhancement of the 808 nm excitation field intensity. On the other hand, OPCs-980 and OPCs-1530 also have a much higher reflectance at ~660 nm than OPCs-808, and thus the enhancement of the ~660 nm UC emission field by OPCs-980 and OPCs-1530 is more obvious. Overall, the combined effect of OPCs-980 or OPCs-1530 on both excitation and emission field enhancement is greater than

https://doi.org/10.1021/acsami.1c21834
ACS Appl. Mater. Interfaces 2022, 14, 428−438

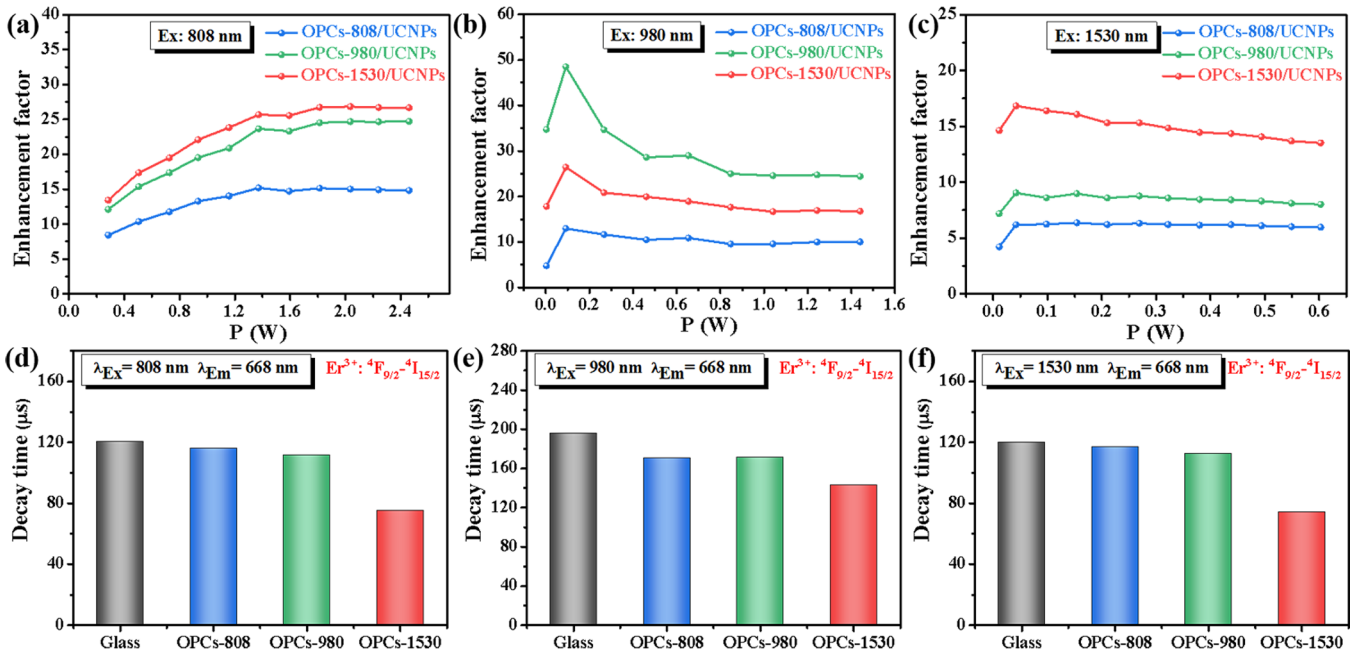

Figure 4. UC emission enhancement factor (EF) versus excitation power measured on the OPCs/UCNPs hybrids under (a) 808 nm, (b) 980 nm, and (c) 1530 nm excitation. (d–f) Decay times of the Er^{3+}:$^4F_{9/2}$ → $^4I_{15/2}$ transition (~668 nm) of $LiErF_4$:0.5%Tm^{3+}@$LiYF_4$ UCNPs on various OPCs/UCNPs hybrids and glass.

Scheme 2. (a) Construction of the Noncontact OPCs/UCNPs Cholesterol Sensor; (b) Schematic Illustration of the Oxidation of Cholesterol Catalyzed by ChOx and Oxidation Color Change of TMB Catalyzed by H_2O_2 in the Presence of HRP; and (c) Principle of the Noncontact Cholesterol Sensor for Cholesterol Detection

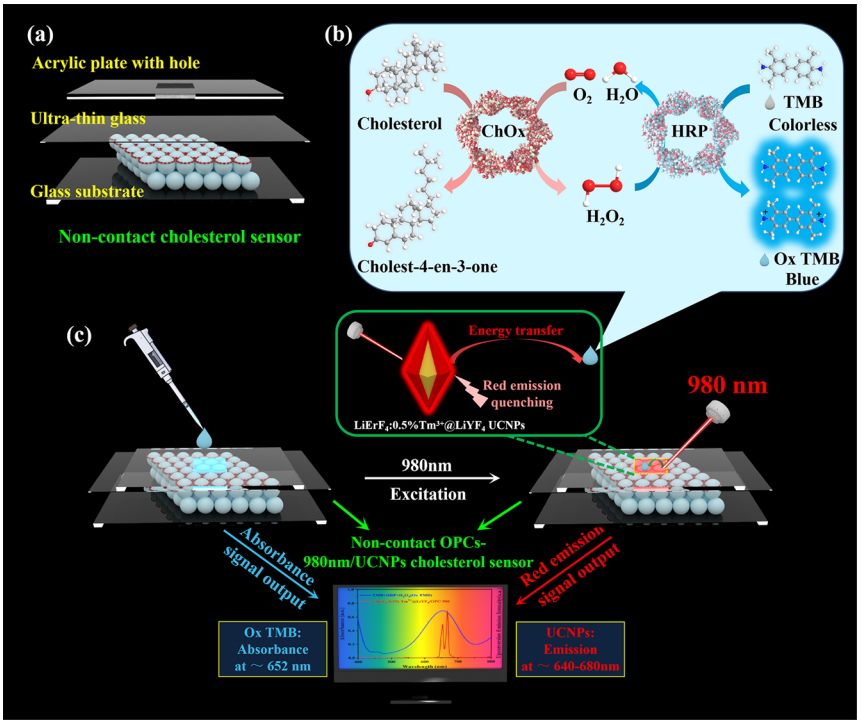

that of OPCs-808 under 808 nm excitation, yielding a stronger red UC emission enhancement.

We further systematically investigated the red UC emission of OPCs/UCNPs composite films as a function of 980 nm excitation power. Typically, the red UC emission integrated intensity (I_{up}) (the integrated range is ~640–680 nm) is proportional to the n^{th} power (P) of pumping power, which could be defined as $I_{up} \propto P^n I_{up} \propto P^n$. n represents the number of infrared photons to be absorbed to emit a visible photon. Figure 3f is the log–log plot of red UC emission integrated intensity as a function of the pumping power of $LiErF_4$:0.5% Tm^{3+}@$LiYF_4$ UCNPs on various OPCs under the 980 nm excitation. The plot of log(I_{up}) against log(P) results in a line with slope n. The slope values of OPCs-808/UCNPs, OPCs-

https://doi.org/10.1021/acsami.1c21834
ACS Appl. Mater. Interfaces 2022, 14, 428–438

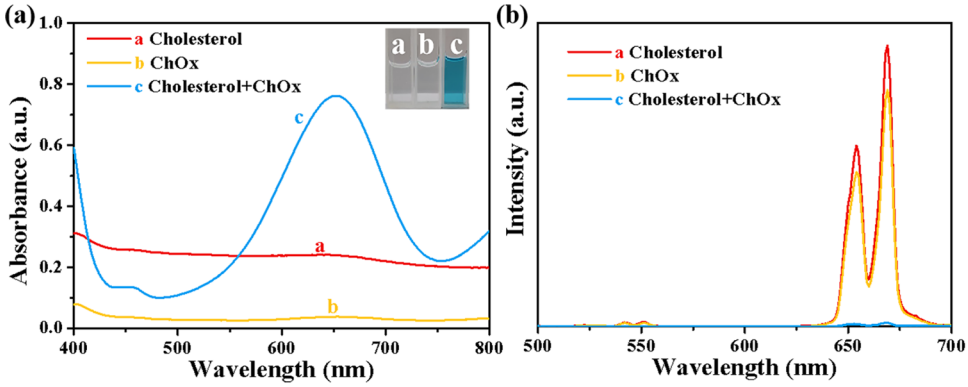

Figure 5. (a) Absorbance and (b) UC emission spectra under 980 nm excitation (6.68 W cm^{-2}) of different reaction systems (note: all systems contain TMB + HRP + H_2O_2 substrates) for demonstrating the feasibility of the cholesterol test. (Inset: The corresponding photographs of different reaction systems).

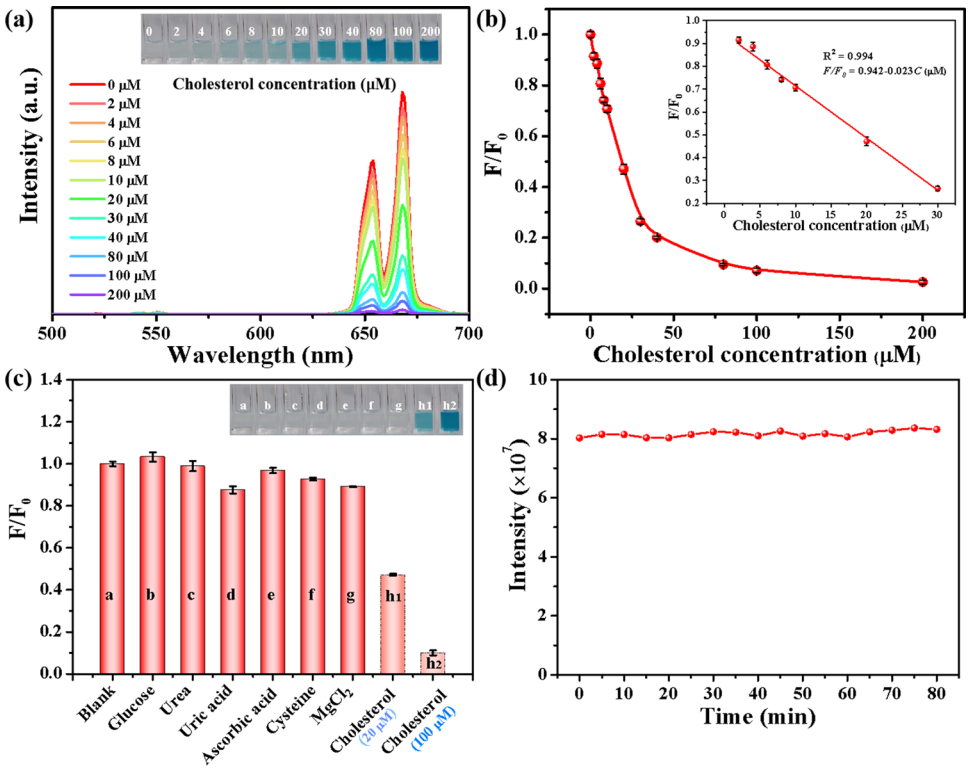

Figure 6. (a) Plot of the UC emission change of $LiErF_4$:0.5%Tm^{3+}@$LiYF_4$ UCNPs on the biosensor versus the concentration of cholesterol from 2 to 200 μM under the 980 nm excitation (6.68 W cm^{-2}). The inset shows the corresponding photographs of the colored products. (b) Plot of F/F_0 of $LiErF_4$:0.5%Tm^{3+}@$LiYF_4$ UCNPs on the sensor at ~640−680 nm versus the concentration of cholesterol from 2 to 200 μM under the 980 nm excitation (6.68 W cm^{-2}). The inset shows the linear curve for cholesterol detection in the range 2−30 μM. (c) F/F_0 of $LiErF_4$:0.5%Tm^{3+}@$LiYF_4$ UCNPs on the sensor with different substances for verifying the selectivity of the sensor. The concentrations were 20 μM and 100 μM for cholesterol and 2 mM for the other interfering substances. The inset shows the corresponding photographs of the solutions containing different substrates. (d) Photostability of the noncontact biosensor under 980 nm (6.68 W cm^{-2}) excitation within 80 min.

980/UCNPs, and OPCs-1530/UCNPs are 1.12, 0.94, and 1.00, respectively. All values of n are far smaller than the required photon numbers ($n \approx 2$) to populate the corresponding levels, which can be ascribed to the saturation effect as well as the local thermal effect caused by laser irradiation.[38−40] Under a comparatively weak excitation power, the intermediate state has a linear decay rate much higher than the UC rate, and the saturation effect does not occur. At this point, the UC rate of the intermediate state is proportional to the excitation power and the EF value gradually increases with the increase in excitation power. Once the excitation power is sufficiently high, the saturation effect occurs, leading to the EF values tending to stabilize or even decrease with the increase in the excitation power, as shown in Figure 4a−c. It also directly demonstrates the existence of the local thermal effect with the increase in excitation power.[39,40]

In addition, to further explore the nature of the PBG on the UC fluorescence enhancement, we measured the fluorescence decay times of the $^4F_{9/2} \rightarrow {}^4I_{15/2}$ transition of Er^{3+} on all OPCs/UCNPs composite films and glass substrates at room temperature under 808, 980, and 1530 nm excitation, respectively, as shown in Figure 4d−f. The decay times of

https://doi.org/10.1021/acsami.1c21834
ACS Appl. Mater. Interfaces 2022, 14, 428−438

the $^4F_{9/2} \rightarrow {}^4I_{15/2}$ transition of Er^{3+} on all OPCs/UCNPs composite films were reduced to different degrees compared to that on the glass substrate. It is noteworthy that the UC luminescence intensity is enhanced, while the lifetime becomes shorter. This is because the luminescence becomes stronger due to the enhancement of the excitation field caused by the photonic crystal effect, but simultaneously, the enhancement of the excitation field induces a local thermal effect, which results in a significant increase in the nonradiative transition rate of $LiErF_4$:0.5%Tm^{3+}@$LiYF_4$ UCNPs. As a result, the luminescence decay process of the UCNPs on the OPCs/UCNPs films is accelerated and the decay time is reduced.

3.4. Detection of Cholesterol by the Noncontact OPCs-980/UCNPs Cholesterol Sensor. Based on the 48.5-fold red UC emission enhancement performance of the OPCs-980/UCNPS composite, as a proof-of-principle demonstration, we further constructed a noncontact sensor for cholesterol detection, as shown in Scheme 2a. The cholesterol can be catalyzed by ChOx to generate hydrogen peroxide (H_2O_2) and choleste-4-en-3-one. The resulting H_2O_2 could oxidize the colorless TMB to the blue oxidization product (Ox TMB) catalyzed by HRP. The Ox TMB exhibits an intense absorption at ~652 nm, which overlaps with the monochromic red UC emission of $LiErF_4$:0.5%Tm^{3+}@$LiYF_4$ UCNPs, as shown in Figure S3. Thus, the monochromic red UC emission could be quenched by Ox TMB, and the intensity of red UC emission quenched by Ox TMB is proportional to the cholesterol concentration, as shown in Scheme 2b,c. Based on this principle, a highly sensitive detection of cholesterol could be achieved. In addition, this noncontact design makes the sensor durable, reusable, and noncontaminating to biological samples, which is desirable for detecting biomolecules in fluids.

We first measured the absorption spectra of various mixture solutions. As shown in Figure 5a, the mixture has a high absorbance at ~652 nm only when cholesterol and ChOx coexisted with the TMB-HRP system, which is due to the formation of Ox TMB. The formation and absorption of Ox TMB led to a significant decrease in the red UC emission of the sensor (Figure 5b).

Based on the above conditions, the cholesterol quantification was performed by detecting the red UC emission of the sensor containing different cholesterol concentrations (2−200 μM), as shown in Figure 6a. As the cholesterol concentration increases, the red UC emission of the $LiErF_4$:0.5%Tm^{3+}@$LiYF_4$ UCNPs is gradually quenched. The relative intensity F/F_0 of the red UC emission in a range of 2−30 μM shows a good linear relationship with the cholesterol concentration (R^2 = 0.994), satisfying the equation $F/F_0 = 0.942 - 0.023C$ (μM). F/F_0 is the ratio of the red UC emission integrated intensity (the integrated range is ~640−680 nm) with different cholesterol concentrations to the luminescence intensity without cholesterol. C represents the concentration of cholesterol (μM). The limit of detection (LOD) for the cholesterol assay is 1.6 μM (LOD = $3\sigma/|K|$). σ is the relative standard deviation obtained from 20 blank tests, and $|K|$ is the absolute value of the slope of the fitted curve. Compared to other methods for cholesterol detection, our method has a higher sensitivity with a LOD as low as 1.6 μM, as shown in Table 1.

Subsequently, to test the selectivity of our sensor, various interferences such as glucose, urea, uric acid, ascorbic acid, cysteine, and $MgCl_2$ were added to the solution instead of cholesterol to test the quenching degree of the red UC emission of UCNPs. As shown in Figure 6c, we can easily distinguish the difference in color with the naked eye (inset). Also, only the addition of cholesterol (20 or 100 μM) can significantly quench the red UC emission, while other interferences have little effect, even if their concentration (2 mM) is 100 or 20 times higher than that of cholesterol. This suggests that our sensor can be used for highly selective cholesterol detection.

Photostability is one of the most important factors in measuring the properties of a device. Therefore, we have also tested the photostability of the sensor under prolonged irradiation with 980 nm laser (6.68 W cm^{-2}). As shown in Figure 6d, the UC emission spectra of the biosensor were tested at 5 min intervals over 80 min. It can be seen that the red UC emission integrated intensity of the UCNPs at ~640−680 nm does not fluctuate significantly with the duration of 980 nm laser irradiation, which indicates the good photostability of the sensor.

We further applied the designed sensor to the detection of cholesterol in actual serum samples, and we collected sera from three patients for the cholesterol assay by our method. The concentrations of cholesterol were calculated according to the linear regression equation $F/F_0 = 0.942 - 0.023C$ (μM), as shown in Table 2, with a relative standard deviation of no more than 11.00% compared to the clinical diagnostic data (obtained by an enzyme-linked immunosorbent assay (ELISA)). These results indicate that our sensor is an effective and reliable method for the determination of cholesterol in complex serum samples, providing a highly sensitive and alternative tool for clinical cholesterol detection.

Table 1. Performance Comparison of Various Cholesterol Sensors

sensors	detection techniques	detection range (μM)	limit of detection (μM)	ref
PB/ChOx/GRE	amperometric	50−800	3.7	6
CS/ChOx/Au NPs/ITO	amperometric	1−45	0.5	5
MoS_2 NRs−Au NPs	colorimetry	400−1000	15	41
graphene quantum dots	colorimetry	20−600	6	1
Fe_3O_4 magnetic nanoparticles	colorimetry	2−50	0.8	42
Mo, S co-doped carbon quantum dots	colorimetry	10−600	7	43
Fe_3O_4@C/Ni nanotubes	colorimetry	5−200	0.17	2
polypyrrole nanoparticles	colorimetry	10−100	3.5	3
bio@AgNP nanohybrids	fluorescence	1−40	5.50	44
noncontact cholesterol sensor	fluorescence	2−30	1.6	this work

Table 2. Determination of Total Cholesterol in Serum

sample	clinical data (mM)	this method (mM) (mean, n = 3)	relative deviation (100%)
Serum 1	4.49	4.78 ± 0.18	6.46
Serum 2	6.39	6.98 ± 0.24	9.24
Serum 3	5.29	5.71 ± 0.24	10.80

https://doi.org/10.1021/acsami.1c21834
ACS Appl. Mater. Interfaces 2022, 14, 428−438

4. CONCLUSIONS

In summary, we have chosen $LiErF_4$:0.5%Tm^{3+}@$LiYF_4$ UCNPs compounded with photonic crystals to investigate the influence of photonic crystal effects on UC luminescence. The unique multi-wavelength excitation (~808, ~980, and ~1530 nm) property of UCNPs allows us to selectively tune the coupling of the PBG with the excitation field to modulate the UC luminescence. When the excitation field wavelength is well matched to the PBG position of the OPCs, maximum EF values of 48.5 and 16.8 times were obtained for OPCs-980 and OPCs-1530 under 980 and 1530 nm excitation, respectively. The enhancement is dominated by the strong coupling between the photonic band gap and the excitation field. At 808 nm excitation, although the PBG position of OPCs-808 well matched the excitation field wavelength, the high reflectance of the OPCs-980 and OPCs-1530 photonic crystals at ~808 and ~660 nm resulted in a greater combined effect of excitation and emission field enhancement than for OPCs-808, yielding a stronger red UC emission enhancement. Based on the 48.5-fold red UC emission enhancement performance of the OPCs-980/UCNPS composite, combined with the cholesterol cascade reactions, we developed a noncontact sensor for the sensitive and selective determination of cholesterol. The assay showed good linearity in the range of 2−30 μM with an LOD of 1.6 μM at 980 nm excitation. In addition, the method has been successfully used for patients' cholesterol detection with results highly consistent with clinical diagnostic data, indicating that this photonic crystal-enhanced upconversion luminescence biosensor could have broad potential in the biological and analytical fields.

■ ASSOCIATED CONTENT

Supporting Information

The Supporting Information is available free of charge at https://pubs.acs.org/doi/10.1021/acsami.1c21834.

Detailed materials and instruments of synthesis and characterizations; upconversion emission spectra of UCNPs under 808 nm excitation (Figure S1); upconversion emission spectra of UCNPs under 1530 nm excitation (Figure S2); and UV−Vis absorption spectrum of Ox TMB and UC emission spectrum of OPCs-980/UCNPs (Figure S3) (PDF)

■ AUTHOR INFORMATION

Corresponding Authors

Xiaomin Liu − *State Key Laboratory of Integrated Optoelectronics, College of Electronic Science and Engineering, Jilin University, Changchun 130012, People's Republic of China;* orcid.org/0000-0003-4186-9637; Email: xiaominliu@jlu.edu.cn

Biao Dong − *State Key Laboratory of Integrated Optoelectronics, College of Electronic Science and Engineering, Jilin University, Changchun 130012, People's Republic of China;* orcid.org/0000-0002-5274-1703; Email: dongb@jlu.edu.cn

Geyu Lu − *State Key Laboratory of Integrated Optoelectronics, College of Electronic Science and Engineering, Jilin University, Changchun 130012, People's Republic of China;* orcid.org/0000-0002-7428-2456; Email: lugy@jlu.edu.cn

Authors

Ling Zhang − *State Key Laboratory of Integrated Optoelectronics, College of Electronic Science and Engineering, Jilin University, Changchun 130012, People's Republic of China*

Songtao Hu − *State Key Laboratory of Integrated Optoelectronics, College of Electronic Science and Engineering, Jilin University, Changchun 130012, People's Republic of China*

Yang Lu − *State Key Laboratory of Integrated Optoelectronics, College of Electronic Science and Engineering, Jilin University, Changchun 130012, People's Republic of China*

Bin Jiang − *State Key Laboratory of Integrated Optoelectronics, College of Electronic Science and Engineering, Jilin University, Changchun 130012, People's Republic of China*

Xiaodan Li − *Department of Respiratory Medicine, The First Hospital, Jilin University, Changchun 130021, People's Republic of China*

Xu Zhao − *State Key Laboratory of Integrated Optoelectronics, College of Electronic Science and Engineering, Jilin University, Changchun 130012, People's Republic of China*

Xu Yan − *State Key Laboratory of Integrated Optoelectronics, College of Electronic Science and Engineering, Jilin University, Changchun 130012, People's Republic of China;* orcid.org/0000-0003-2152-675X

Chenguang Wang − *State Key Laboratory of Integrated Optoelectronics, College of Electronic Science and Engineering, Jilin University, Changchun 130012, People's Republic of China;* orcid.org/0000-0001-9770-1062

Xiaoteng Jia − *State Key Laboratory of Integrated Optoelectronics, College of Electronic Science and Engineering, Jilin University, Changchun 130012, People's Republic of China;* orcid.org/0000-0001-5630-8838

Fengmin Liu − *State Key Laboratory of Integrated Optoelectronics, College of Electronic Science and Engineering, Jilin University, Changchun 130012, People's Republic of China;* orcid.org/0000-0003-1523-2915

Complete contact information is available at: https://pubs.acs.org/10.1021/acsami.1c21834

Author Contributions

‡L.Z. and S.T.H. contributed equally to this work. The manuscript was written through contributions of all authors. All authors have given approval to the final version of the manuscript.

Notes

The authors declare no competing financial interest.

■ ACKNOWLEDGMENTS

This work is supported by the National Natural Science Foundation of China (nos. 61875191, U2003127, 62171194, 11874354, and 21902057).

■ REFERENCES

(1) Nirala, N. R.; Abraham, S.; Kumar, V.; Bansal, A.; Srivastava, A.; Saxena, P. S. Colorimetric Detection of Cholesterol Based on Highly Efficient Peroxidase Mimetic Activity of Graphene Quantum Dots. *Sens. Actuators, B* **2015**, *218*, 42−50.

(2) Peng, H.; Zhang, J.; Zeng, C.; Zhou, C.; Li, Q.; Lu, N.; Wang, L. One-Dimensional Synergistic Core−Shell Nanozymes with Superior Peroxidase-Like Activity for Ultrasensitive Colorimetric Detection of Blood Cholesterol. *ACS Appl. Bio Mater.* **2020**, *3*, 5111−5119.

(3) Hong, C.; Zhang, X.; Wu, C.; Chen, Q.; Yang, H.; Yang, D.; Huang, Z.; Cai, R.; Tan, W. On-Site Colorimetric Detection of Cholesterol Based on Polypyrrole Nanoparticles. *ACS Appl. Mater. Interfaces* **2020**, *12*, 54426−54432.
(4) Albuquerque, T. G.; Oliveira, M. B.; Sanches-Silva, A.; Costa, H. S. Cholesterol Determination in Foods: Comparison between High Performance and Ultra-High Performance Liquid Chromatography. *Food Chem.* **2016**, *193*, 18−25.
(5) Gomathi, P.; Ragupathy, D.; Choi, J. H.; Yeum, J. H.; Lee, S. C.; Kim, J. C.; Lee, S. H.; Ghim, H. D. Fabrication of Novel Chitosan Nanofiber/Gold Nanoparticles Composite towards Improved Performance for a Cholesterol Sensor. *Sens. Actuators, B* **2011**, *153*, 44−49.
(6) Sekretaryova, A. N.; Beni, V.; Eriksson, M.; Karyakin, A. A.; Turner, A. P.; Vagin, M. Y. Cholesterol Self-Powered Biosensor. *Anal. Chem.* **2014**, *86*, 9540−9547.
(7) Gao, Y.; Wu, Y.; Zhao, K.; Wang, H.; Liu, S. In-Situ Imaging Detection of Cell Membrane and Intracellular Cholesterol via Cascade Reactions. *Biosens. Bioelectron.* **2019**, *126*, 249−254.
(8) Mondal, A.; Jana, N. R. Fluorescent Detection of Cholesterol Using Beta-Cyclodextrin Functionalized Graphene. *Chem. Commun.* **2012**, *48*, 7316−7318.
(9) Ding, Y.; Zhu, H.; Zhang, X.; Gao, J.; Abdel-Halim, E. S.; Jiang, L.; Zhu, J. J. An Upconversion Nanocomposite for Fluorescence Resonance Energy Transfer Based Cholesterol-Sensing in Human Serum. *Nanoscale* **2014**, *6*, 14792−14798.
(10) Chang, H. C.; Ho, J. A. Gold Nanocluster-Assisted Fluorescent Detection for Hydrogen Peroxide and Cholesterol Based on the Inner Filter Effect of Gold Nanoparticles. *Anal. Chem.* **2015**, *87*, 10362−10367.
(11) Su, Q.; Gan, L.; Zhu, Y.; Yang, X. Dual-Emissive Fluorescence and Phosphorescence Detection of Cholesterol and Glucose Based on Carbon Dots-Cyanuric Acid Complex Quenched by MnO_2 Nanosheets. *Sens. Actuators, B* **2021**, *335*, 129715.
(12) Wang, K.; Ren, H.; Li, N.; Tan, X.; Dang, F. Ratiometric Fluorescence Sensor Based on Cholesterol Oxidase-Functionalized Mesoporous Silica Nanoparticle@ZIF-8 Core-Shell Nanocomposites for Detection of Cholesterol. *Talanta* **2018**, *188*, 708−713.
(13) Sun, L.; Li, S.; Ding, W.; Yao, Y.; Yang, X.; Yao, C. Fluorescence Detection of Cholesterol Using a Nitrogen-Doped Graphene Quantum Dot/Chromium Picolinate Complex-Based Sensor. *J. Mater. Chem. B* **2017**, *5*, 9006−9014.
(14) Ma, W.; Fu, P.; Sun, M.; Xu, L.; Kuang, H.; Xu, C. Dual Quantification of MicroRNAs and Telomerase in Living Cells. *J. Am. Chem. Soc.* **2017**, *139*, 11752−11759.
(15) Chen, X.; Zhang, X.; Zhang, L.; Gao, Y.; Wang, C.; Hong, W.; Zhao, G.; Li, L.; Liu, R.; Wang, C. Amphiphilic Janus Nanoparticles for Imaging-Guided Synergistic Chemo-Photothermal Hepatocellular Carcinoma Therapy in the Second Near-Infrared Window. *Nanoscale* **2021**, *13*, 3974−3982.
(16) Jia, T.; Wang, Q.; Xu, M.; Yuan, W.; Feng, W.; Li, F. Highly Efficient BODIPY-Doped Upconversion Nanoparticles for Deep-Red Luminescence Bioimaging in vivo. *Chem. Commun.* **2021**, *57*, 1518−1521.
(17) Huo, M.; Liu, P.; Zhang, L.; Wei, C.; Wang, L.; Chen, Y.; Shi, J. Upconversion Nanoparticles Hybridized Cyanobacterial Cells for Near-Infrared Mediated Photosynthesis and Enhanced Photodynamic Therapy. *Adv. Funct. Mater.* **2021**, *31*, 2010196.
(18) Zhang, Z. M.; Shikha, S.; Liu, J. L.; Zhang, J.; Mei, Q. S.; Zhang, Y. Upconversion Nanoprobes: Recent Advances in Sensing Applications. *Anal. Chem.* **2019**, *91*, 548−568.
(19) Zhang, G.; Yang, Y.; Shi, J.; Yao, X.; Chen, W.; Wei, X.; Zhang, X.; Chu, P. K. Near-Infrared Light II - Assisted Rapid Biofilm Elimination Platform for Bone Implants at Mild Temperature. *Biomaterials* **2021**, *269*, 120634.
(20) Wang, Z.; Qiu, X.; Xi, W.; Tang, M.; Liu, J.; Jiang, H.; Sun, L. Tailored Upconversion Nanomaterial: a Hybrid Nano Fluorescent Sensor for Evaluating Efficacy of Lactate Dehydrogenase Inhibitors as Anticancer Drugs. *Sens. Actuators, B* **2021**, *345*, 130417.
(21) Wang, F.; Han, Y.; Lim, C. S.; Lu, Y.; Wang, J.; Xu, J.; Chen, H.; Zhang, C.; Hong, M.; Liu, X. Simultaneous Phase and Size Control of Upconversion Nanocrystals through Lanthanide Doping. *Nature* **2010**, *463*, 1061−1065.
(22) Liu, Q.; Sun, Y.; Yang, T.; Feng, W.; Li, C.; Li, F. Sub-10 nm Hexagonal Lanthanide-Doped $NaLuF_4$ Upconversion Nanocrystals for Sensitive Bioimaging in vivo. *J. Am. Chem. Soc.* **2011**, *133*, 17122−17125.
(23) Homann, C.; Krukewitt, L.; Frenzel, F.; Grauel, B.; Wurth, C.; Resch-Genger, U.; Haase, M. $NaYF_4$:Yb,Er/$NaYF_4$ Core/Shell Nanocrystals with High Upconversion Luminescence Quantum Yield. *Am. Ethnol.* **2018**, *57*, 8765−8769.
(24) Johnson, N. J.; Korinek, A.; Dong, C.; van Veggel, F. C. Self-focusing by Ostwald Ripening: a Strategy for Layer-by-layer Epitaxial Growth on Upconverting Nanocrystals. *J. Am. Chem. Soc.* **2012**, *134*, 11068−11071.
(25) Song, Y.; Lu, M.; Mandl, G. A.; Xie, Y.; Sun, G.; Chen, J.; Liu, X.; Capobianco, J. A.; Sun, L. Energy Migration Control of Multimodal Emissions in an Er^{3+}-Doped Nanostructure for Information Encryption and Deep-Learning Decoding. *Am. Ethnol.* **2021**, *60*, 23790−23796.
(26) Liao, J. Y.; Yang, Z. W.; Lai, S. F.; Shao, B.; Li, J.; Qiu, J. B.; Song, Z. G.; Yang, Y. Upconversion Emission Enhancement of $NaYF_4$:Yb,Er Nanoparticles by Coupling Silver Nanoparticle Plasmons and Photonic Crystal Effects. *J. Phys. Chem. C* **2014**, *118*, 17992−17999.
(27) Yin, Z.; Zhu, Y.; Xu, W.; Wang, J.; Xu, S.; Dong, B.; Xu, L.; Zhang, S.; Song, H. Remarkable Enhancement of Upconversion Fluorescence and Confocal Imaging of PMMA Opal/$NaYF_4$:Yb^{3+}, Tm^{3+}/Er^{3+} Nanocrystals. *Chem. Commun.* **2013**, *49*, 3781−3783.
(28) Zhang, H.; Li, Y.; Ivanov, I. A.; Qu, Y.; Huang, Y.; Duan, X. Plasmonic Modulation of the Upconversion Fluorescence in $NaYF_4$:Yb/Tm Hexaplate Nanocrystals Using Gold Nanoparticles or Nanoshells. *Am. Ethnol.* **2010**, *49*, 2865−2868.
(29) Yin, Z.; Li, H.; Xu, W.; Cui, S.; Zhou, D.; Chen, X.; Zhu, Y.; Qin, G.; Song, H. Local Field Modulation Induced Three-Order Upconversion Enhancement: Combining Surface Plasmon Effect and Photonic Crystal Effect. *Adv. Mater.* **2016**, *28*, 2518−2525.
(30) Hu, S.; Xu, H.; Zhou, B.; Xu, S.; Shen, B.; Dong, B.; Yin, Z.; Xu, S.; Sun, L.; Lv, J.; et al. Double Stopband Bilayer Photonic Crystal Based Upconversion Fluorescence PSA Sensor. *Sens. Actuators, B* **2021**, *326*, 128816.
(31) Shi, Y. H.; Zhang, F. Q.; Xu, J.; Zhou, K.; Chen, C.; Cheng, J.; Li, P. Upconversion Fluorescence Enhancement of $NaYF_4$:Yb/Re Nanoparticles by Coupling with SiO_2 Opal Photonic Crystals. *J. Mater. Sci.* **2019**, *54*, 8461−8471.
(32) Zhang, L.; Li, X.; Wang, W.; Zhao, X.; Yan, X.; Wang, C.; Bao, H.; Lu, Y.; Kong, X.; Liu, F.; et al. Construction of Self-Sensitized $LiErF_4$:0. 5% Tm3+@LiYF4 Upconversion Nanoprobe for Trace Water Sensing. *Nano Res.* **2020**, *13*, 2803−2811.
(33) Li, Z.; Zhang, Y. An Efficient and User-Friendly Method for the Synthesis of Hexagonal-Phase $NaYF_4$:Yb, Er/Tm Nanocrystals with Controllable Shape and Upconversion Fluorescence. *Nanotechnology* **2008**, *19*, 345606.
(34) Fenzl, C.; Hirsch, T.; Wolfbeis, O. S. Photonic Crystals for Chemical Sensing and Biosensing. *Am. Ethnol.* **2014**, *53*, 3318−3335.
(35) Stein, A.; Li, F.; Denny, N. R. Morphological Control in Colloidal Crystal Templating of Inverse Opals, Hierarchical Structures, and Shaped Particles. *Chem. Mater.* **2008**, *20*, 649−666.
(36) Fudouzi, H. Fabricating High-Quality Opal Films with Uniform Structure over a Large Area. *J. Colloid Interface Sci.* **2004**, *275*, 277−283.
(37) Romanov, S. G.; Maka, T.; Sotomayor Torres, C. M.; Muller, M.; Zentel, R.; Cassagne, D.; Manzanares-Martinez, J.; Jouanin, C. Diffraction of Light from Thin-Film Polymethylmethacrylate Opaline Photonic Crystals. *Phys. Rev. E* **2001**, *63*, No. 056603.
(38) Pollnau, M.; Gamelin, D. R.; Luthi, S. R.; Gudel, H. U.; Hehlen, M. P. Power Dependence of Upconversion Luminescence in

Lanthanide and Transition-Metal-Ion Systems. *Phys. Rev. B* **2000**, *61*, 3337−3346.
(39) Bai, X.; Song, H. W.; Pan, G. H.; Lei, Y. Q.; Wang, T.; Ren, X. G.; Lu, S. Z.; Dong, B.; Dai, Q. L.; Fan, L. Size-Dependent Upconversion Luminescence in Er^{3+}/Yb^{3+}-codoped Nanocrystalline Yttria: Saturation and Thermal Effects. *J. Phys. Chem. C* **2007**, *111*, 13611−13617.
(40) Li, D.; Dong, B. A.; Bai, X.; Wang, Y.; Song, H. W. Influence of the TGA Modification on Upconversion Luminescence of Hexagonal-Phase $NaYF_4$:Yb^{3+}, Er^{3+} Nanoparticles. *J. Phys. Chem. C* **2010**, *114*, 8219−8226.
(41) Nirala, N. R.; Pandey, S.; Bansal, A.; Singh, V. K.; Mukherjee, B.; Saxena, P. S.; Srivastava, A. Different Shades of Cholesterol: Gold Nanoparticles Supported on MoS_2 Nanoribbons for Enhanced Colorimetric Sensing of Free Cholesterol. *Biosens. Bioelectron.* **2015**, *74*, 207−213.
(42) Wu, Y.; Ma, Y.; Xu, G.; Wei, F.; Ma, Y.; Song, Q.; Wang, X.; Tang, T.; Song, Y.; Shi, M.; et al. Metal-Organic Framework Coated Fe_3O_4 Magnetic Nanoparticles with Peroxidase-Like Activity for Colorimetric Sensing of Cholesterol. *Sens. Actuators, B* **2017**, *249*, 195−202.
(43) Zhao, L.; Wu, Z.; Liu, G.; Lu, H.; Gao, Y.; Liu, F.; Wang, C.; Cui, J.; Lu, G. High-Activity Mo, S Co-Doped Carbon Quantum Dot Nanozyme-Based Cascade Colorimetric Biosensor for Sensitive Detection of Cholesterol. *J. Mater. Chem. B* **2019**, *7*, 7042−7051.
(44) Xu, H. V.; Zhao, Y.; Tan, Y. N. Nanodot-Directed Formation of Plasmonic-Fluorescent Nanohybrids toward Dual Optical Detection of Glucose and Cholesterol via Hydrogen Peroxide Sensing. *ACS Appl. Mater. Interfaces* **2019**, *11*, 27233−27242.

https://doi.org/10.1021/acsami.1c21834
ACS Appl. Mater. Interfaces 2022, 14, 428−438